Acta Crystallographica Section F
Structural Biology and Crystallization Communications
ISSN 1744-3091

Structure of glyceraldehyde-3-phosphate dehydrogenase from the archaeal hyperthermophile *Methanocaldococcus jannaschii*

Ali D. Malay,[a]‡ Yoshitaka Bessho,[a,b] Mark J. Ellis,[c] Svetlana V. Antonyuk,[d] Richard W. Strange,[d] S. Samar Hasnain,[d] Akeo Shinkai,[b] Balasundaram Padmanabhan[a]*§ and Shigeyuki Yokoyama[a,b,e]*

[a]Systems and Structural Biology Center, Yokohama Institute, RIKEN, 1-7-22 Suehiro, Tsurumi, Yokohama 230-0045, Japan, [b]RIKEN SPring-8 Center, Harima Institute, 1-1-1 Kouto, Sayo, Hyogo 679-5148, Japan, [c]STFC Daresbury Laboratory, Warrington, Cheshire WA4 4AD, England, [d]Molecular Biophysics Group, School of Biological Sciences, University of Liverpool, Liverpool L69 7ZB, England, and [e]Department of Biophysics and Biochemistry, Graduate School of Science, The University of Tokyo, Bunkyo-ku, Tokyo 113-0033, Japan

‡ Present address: Global Edge Institute, Tokyo Institute of Technology, 4259, S2-17, Nagatsuda, Midori-ku, Yokohama, Kanagawa 226-8503, Japan.
§ Present address: Aptuit Laurus Private Ltd, ICICI Knowledge Park, Turkapally, Shameerpet, Hyderabad 500 078, India.

Correspondence e-mail: bpadmanabhan@hotmail.com, yokoyama@biochem.s.u-tokyo.ac.jp

Received 25 June 2009
Accepted 7 November 2009

PDB Reference: glyceraldehyde-3-phosphate dehydrogenase, 2yyy, r2yyysf.

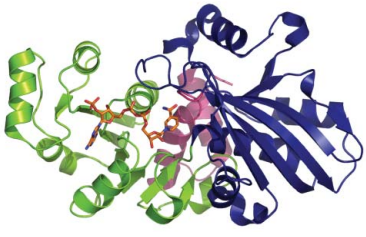

The X-ray crystal structure of glyceraldehyde-3-phosphate dehydrogenase (GAPDH) from the hyperthermophilic archaeon *Methanocaldococcus jannaschii* (Mj-GAPDH) was determined to 1.81 Å resolution. The crystal belonged to space group $C222_1$, with unit-cell parameters $a = 83.4$, $b = 152.0$, $c = 118.6$ Å. The structure was solved by molecular replacement and was refined to a final R factor of 17.1% (R_{free} = 19.8%). The final structure included the cofactor $NADP^+$ at the nucleotide-binding site and featured unoccupied inorganic and substrate phosphate-binding sites. A comparison with GAPDH structures from mesophilic sources suggested that Mj-GAPDH is stabilized by extensive electrostatic interactions between the C-terminal α-helices and various distal loop regions, which are likely to contribute to thermal stability. The key phosphate-binding residues in the active site of Mj-GAPDH are conserved in other archaeal GAPDH proteins. These residues undergo a conformational shift in response to occupancy of the inorganic phosphate site.

1. Introduction

Glyceraldehyde-3-phosphate dehydrogenase (GAPDH; EC 1.2.1.12) catalyzes the reversible oxidative phosphorylation of glyceraldehyde 3-phosphate to 1,3-bisphosphoglycerate in the presence of inorganic phosphate and the cofactor NADH or NADPH as part of the classic pathways of glycolysis and gluconeogenesis (Harris & Waters, 1976). In addition, GAPDH acts as a 'moonlighting enzyme' that has been implicated in diverse cellular pathways ranging from transcriptional activation and membrane trafficking to apoptosis (Sirover, 1999, 2005; Tisdale, 2002; Zheng *et al.*, 2003).

Numerous structures of the highly conserved GAPDH proteins from bacteria and eukaryotes have been characterized (Murthy *et al.*, 1980; Skarzynski *et al.*, 1987; Duée *et al.*, 1996; Tanner *et al.*, 1996; Antonyuk *et al.*, 2003). In addition, several GAPDH structures from archaea have been reported (Isupov *et al.*, 1999; Charron *et al.*, 2000). The archaeal GAPDHs belong to a different class to their bacterial/eukaryotic counterparts. Although the two classes share a similar basic architecture, the archaeal GAPDHs exhibit some distinct characteristics such as the translocation of important active-site residues to different structural elements and the presence of extra secondary-structure elements. The evolutionary relationship between the archaeal and bacterial/eukaryotic GAPDHs is still an open question (Arcari *et al.*, 1993; Littlechild *et al.*, 2004).

In this study, we report the crystal structure of GAPDH from the hyperthermophilic archaeon *Methanocaldococcus jannaschii* (Mj-GAPDH) determined at 1.81 Å resolution.

2. Materials and methods

2.1. Cloning, expression and purification

The gene encoding the Mj-GAPDH protein (gi:15669333) was amplified *via* PCR using *M. jannaschii* DSM 2661 genomic DNA and was cloned into the pET-21a expression vector (Merck Novagen, Darmstadt, Germany). The expression vector was introduced into *Escherichia coli* BL21-CodonPlus(DE3)-RIL strain (Stratagene, La Jolla, California, USA) and the recombinant strain was cultured

in 4.5 l LB medium containing 30 µg ml^{-1} chloramphenicol and 50 µg ml^{-1} ampicillin. The harvested cells (16.3 g) were lysed by sonication in 30 ml 20 m*M* Tris–HCl buffer pH 8.0 containing 500 m*M* NaCl, 5 m*M* β-mercaptoethanol and 1 m*M* phenylmethylsulfonyl fluoride on ice. The cell lysate was heat-treated at 343 K for 13 min and centrifuged at 15 000*g* for 30 min at 277 K. The supernatant was desalted by fractionation on a HiPrep 26/10 column (GE Healthcare Biosciences). The sample was applied onto a Toyopearl SuperQ-650M column (Tosoh, Tokyo) equilibrated with 20 m*M* Tris–HCl buffer pH 8.0 and was eluted with a linear (0–0.3 *M*) gradient of NaCl. The target sample, which eluted in the 0.26 *M* NaCl fraction, was then applied onto a Resource Q column (GE Healthcare Biosciences) equilibrated with 20 m*M* Tris–HCl buffer pH 8.0 and was eluted with a linear gradient of 0–0.5 *M* NaCl. The fractions that eluted in 0.33 *M* NaCl were further purified using a hydroxyapatite CHT20-I column (Bio-Rad Laboratories) with a linear gradient of 0.01–0.5 *M* potassium phosphate buffer pH 7.0. The target sample, which eluted in the 0.09 *M* potassium phosphate fraction, was concentrated and applied onto a HiLoad 16/60 Superdex 200 pg column (GE Healthcare Biosciences) equilibrated with 20 m*M* Tris–HCl buffer pH 8.0 containing 200 m*M* NaCl. The protein sample was analyzed by SDS–PAGE and was confirmed by N-terminal amino-acid sequencing. After concentration to approximately 20 mg ml^{-1} by ultrafiltration, the protein yield was 26.2 mg from 16.3 g of cells.

2.2. Protein crystallization

Crystallization was performed using the microbatch-under-oil method at 291 K. 0.5 µl crystallization reagent was mixed with 0.5 µl 23.2 mg ml^{-1} protein solution and was covered with 15 µl silicone and paraffin oil. In the preliminary screen, small crystals appeared using a crystallization reagent consisting of 0.08 *M* Tris–HCl buffer pH 8.5 containing 24%(*w*/*v*) PEG 4000, 0.16 *M* magnesium chloride hexahydrate and 20%(*v*/*v*) anhydrous glycerol (Crystal Screen Cryo condition No. 6, Hampton Research). After optimization, large crystals were obtained from a crystallization reagent consisting of 0.08 *M* Tris–HCl buffer pH 8.5 containing 24%(*w*/*v*) PEG 4000, 0.2 *M* magnesium chloride hexahydrate and 20%(*v*/*v*) anhydrous glycerol. Crystals suitable for X-ray data collection appeared within 2 d and reached final dimensions of 0.6 × 0.04 × 0.02 mm (Fig. 1). The crystals were flash-cooled in a nitrogen-gas stream at 100 K without additional cryoprotectants.

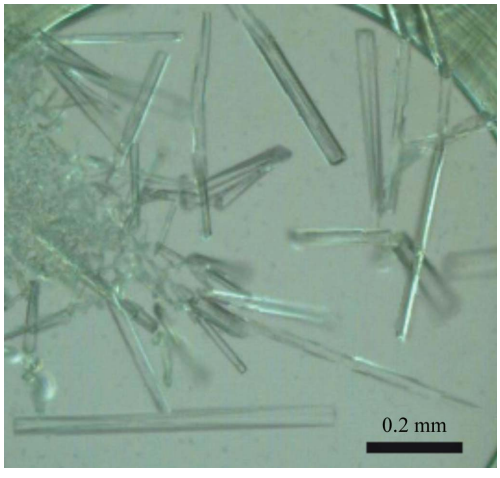

Figure 1
Crystal morphology. Crystals of Mj-GAPDH prior to flash-cooling in glycerol cryoprotectant.

Table 1
X-ray data-collection and refinement statistics.

Values in parentheses are for the highest resolution shell.

Data collection	
X-ray source	SRS PX10.1
Wavelength (Å)	1.117
Space group	$C222_1$
Unit-cell parameters (Å, °)	a = 83.4, b = 152.04, c = 118.55, $\alpha = \beta = \gamma = 90$
Matthews coefficient (Å^3 Da^{-1})	2.46
Solvent content (%)	50.0
Wilson B factor (Å^2)	17.2
No. of unique reflections	62507 (4944)
$R_{\rm merge}$†	0.066 (0.238)
Redundancy	4.5 (2.9)
Completeness (%)	97.1 (78.1)
$I/\sigma(I)$	13.5 (4.2)
Refinement	
Resolution (Å)	20–1.85
R factor/$R_{\rm free}$‡ (%)	0.171 (0.198)
No. of protein atoms	5328
No. of ligand atoms	96
No. of water atoms	348
R.m.s. deviations from ideality	
Bond lengths (Å)	0.016
Bond angles (°)	1.5
Ramachandran plot (%)	
Most favoured regions	91.8
Additional allowed regions	7.9
Generously allowed regions	0.3
Average B values (Å^2)	
Overall	18.8
Protein atoms	18.4
Ligand atoms	20.9

† $R_{\rm merge} = \sum_{hkl}\sum_i |I_i(hkl) - \langle I(hkl)\rangle| / \sum_{hkl}\sum_i I_i(hkl)$, where $I_i(hkl)$ is the intensity of the ith measurement of reflection hkl and $\langle I(hkl)\rangle$ is the average value over multiple measurements. ‡ R factor $= \sum_{hkl} \big||F_{\rm obs}| - |F_{\rm calc}|\big| / \sum_{hkl} |F_{\rm obs}|$, where $F_{\rm obs}$ and $F_{\rm calc}$ are the observed and calculated structure factors, respectively. $R_{\rm free}$ was calculated for 5% of the reflections removed randomly from the refinement.

2.3. Structure determination and refinement

Experiments were performed on beamline 10.1 at the Daresbury Synchrotron Radiation Source (SRS), employing a Si(111) sagittally focused monochromator and a MAR Mosaic 225 CCD detector. The data-collection and refinement parameters are summarized in Table 1. Indexing and scaling of the reflection data were performed using the *HKL*-2000 software package (Otwinowski & Minor, 1997). Molecular replacement was accomplished using the program *MOLREP* (Vagin & Teplyakov, 1997) from the *CCP*4 program suite. The monomeric structure of *Methanothermus fervidus* GAPDH (Mf-GAPDH; PDB code 1cf2; Charron *et al.*, 2000) was used as the initial search model. The molecular-replacement solution was subsequently used in automated model building *via ARP*/*wARP* (Lamzin & Wilson, 1993). Further iterative rounds of refinement and model building were performed using *REFMAC*5 (Murshudov *et al.*, 1997) and *O* (Jones *et al.*, 1991). Noncrystallographic symmetry restraints were not employed during refinement. The structure was validated using *MolProbity* (Davis *et al.*, 2004) and was deposited in the PDB under accession code 2yyy. All structure images were generated using *PyMOL* (DeLano, 2002).

3. Results

3.1. Overall structure of Mj-GAPDH

The final model contains two molecules of Mj-GAPDH in the asymmetric unit, which contains a total of 684 amino-acid residues. The first residue, Met1, appears to have been cleaved off from the protein. The two monomers, *A* and *B*, have a root-mean-square

deviation (r.m.s.d.) value of 0.11 Å for C^{α} positions along the entire sequence. Although it was not added separately to the sample, the $NADP^{+}$ cofactor is clearly visible as electron density within the putative nucleotide-binding site of each GAPDH monomer. There are 348 water molecules in the model, with no additional anions at the known P_i (inorganic phosphate) and P_s (substrate phosphate) binding sites.

The overall architecture of the Mj-GAPDH monomer is typical of archaeal GAPDH proteins and comprises three domains, a nucleotide-binding domain (NBD; residues 1–142), a catalytic domain (CAD; 143–305) and a C-terminal domain (CTD; 306–343), as shown in Figs. 2 and 3(*a*). The N-terminal NBD consists of a parallel β-sheet surrounded by α-helices in a classical Rossmann fold (sheets βA–βF and helices αA–αG). The CAD is composed of an antiparallel β-sheet surrounded by α-helices (sheets $\beta1$–$\beta8$ and helices $\alpha1$–$\alpha4'$). This domain contains the active-site residues, as well as the so-called S-loop between $\beta1$ and $\beta2$ (residues 173–187). The relatively short CTD, composed of the two helices αH and αJ, is located at the junction between the NBD and CAD. It should be noted that in previous studies the C-terminal region has been treated as part of the NBD; however, for the sake of clarity, we are evaluating the CTD as a separate domain. The three proline residues, Pro183 in the S-loop and Pro191 and Pro195 in the loop following $\beta2$, are in the *cis* configuration and two of them (Pro183 and Pro195) are conserved across all GAPDH species.

Ramachandran plot analysis revealed that 91.8% of the residues are in the most favoured regions and 7.9% are in additional favoured regions, while 0.3% are in generously allowed regions. One residue, Lys92, falls into the disallowed region in both monomers. A closer inspection revealed that this surface residue is constrained owing to the effects of crystal packing. The average *B* factor is 18.8 $Å^2$ for the overall structure.

3.2. Comparison with GAPDH structures from other sources

The primary sequence alignment of Mj-GAPDH with GAPDH proteins from other sources is shown in Fig. 2. Three other archaeal GAPDH proteins with known structures are represented: those from

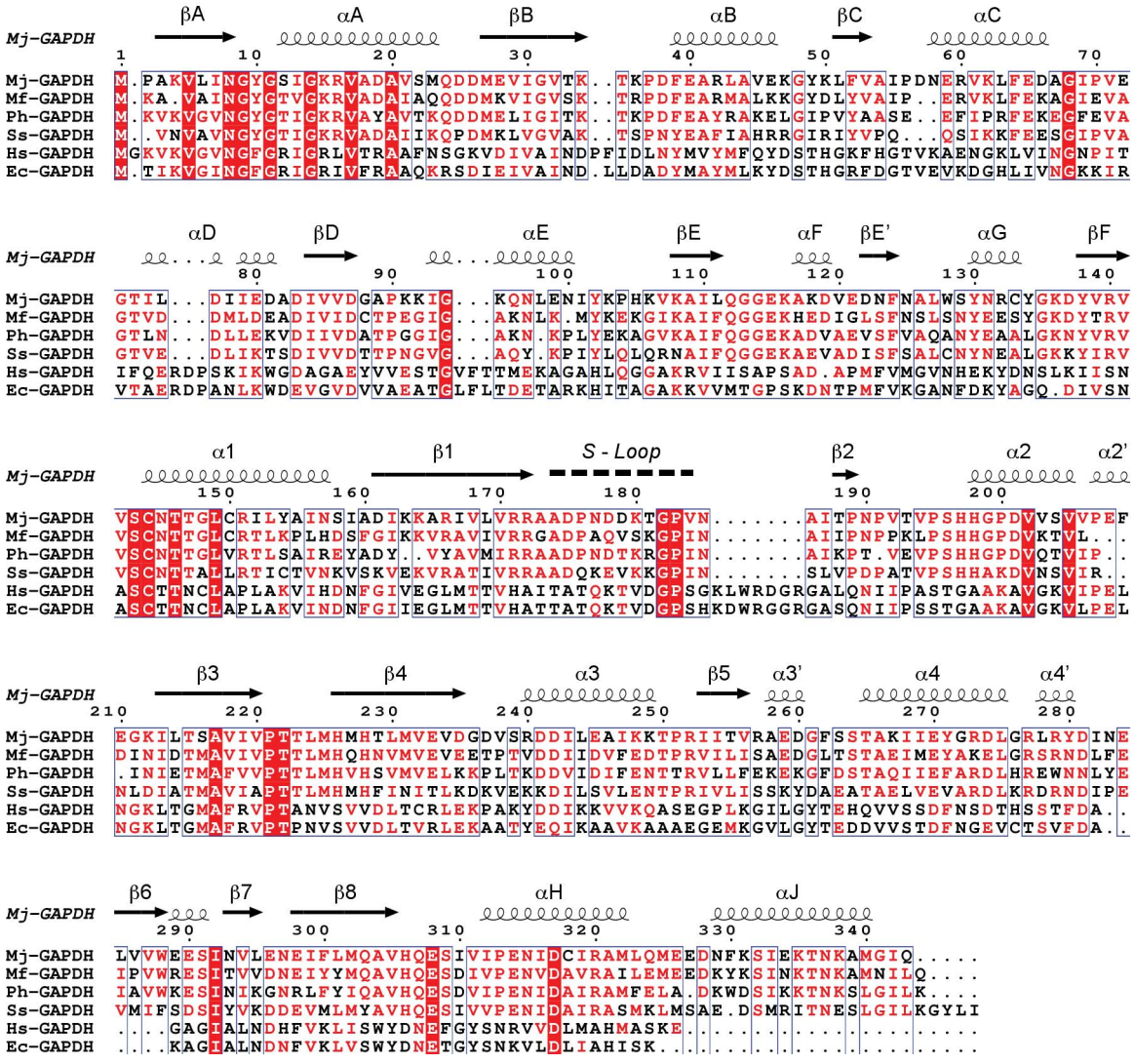

Figure 2
The sequence alignment between Mj-GAPDH and orthologs from other species: Mf-GAPDH, archaeal *M. fervidus*; Ph-GAPDH, archaeal *P. horikoshii*; Ss-GAPDH, archaeal *S. solfataricus*; Ec-GAPDH, bacterial *E. coli*; Hs-GAPDH, eukaryotic human liver. Regions of similarity are in blue boxes, with the strictly conserved residues highlighted in red. The secondary-structure elements of Mj-GAPDH are indicated above the alignment. The naming of the secondary structural elements follows that of Charron *et al.* (2000)

the hyperthermophilic *Methanothermus fervidus* (Mf-GAPDH), *Pyrococcus horikoshii* (Ph-GAPDH) and *Sulfolobus solfataricus* (Ss-GAPDH). In addition, the bacterial *E. coli* (Ec-GAPDH) and human liver (Hs-GAPDH) GAPDH sequences are shown for comparison. The alignments revealed that Mj-GAPDH shares 59, 53 and 46% overall amino-acid sequence identity with the archaeal Mf-GAPDH, Ph-GAPDH and Ss-GAPDH, respectively. Superposition of the C^{α} positions of the Mj-GAPDH monomer structure with the archaeal GAPDH structures Mf-GAPDH, Ph-GAPDH and Ss-GAPDH yielded r.m.s.d. values of 0.51, 0.72 and 0.82 Å, respectively (Fig. 3*b*). The regions with the greatest divergence in the main-chain positions include αC and the loop preceding it, the loop $\beta7$–$\beta8$ and the $\alpha2$–$\alpha2'$ region. The bacterial and eukaryotic GAPDH protein sequences are more closely related to each other than to the archaeal GAPDHs. Mj-GAPDH shares only 19 and 18% global sequence identity with Ec-GAPDH and Hs-GAPDH, respectively. Although the archaeal and bacterial/eukaryotic GAPDH proteins share some basic structural features, notably the core β-sheet NBD and CAD regions, prominent differences include the presence of shorter loops in the archaeal GAPDHs, including an S-loop that is shorter by seven residues. In addition, the archaeal GAPDHs feature some extra α-helical elements, including the αC helix, a much longer $\alpha4$ helix and the presence of the C-terminal helix αJ, which is completely absent from the bacterial and eukaryotic GAPDHs. Although the archaeal and bacterial/eukaryotic GAPDHs share similar active sites and cofactor-binding sites, several key residues are translocated to different secondary-structural sites in the two classes of GAPDHs, as discussed by Littlechild *et al.* (2004).

3.3. Quaternary structure

The tetramer is generated from the two monomers of Mj-GAPDH in the asymmetric unit (chains *A* and *B*) by applying a twofold symmetry operation, resulting in four GAPDH monomers arranged with 222 point symmetry (Fig. 3*c*). The Mj-GAPDH tetramer corresponds closely to the quaternary arrangement found in other archaeal GAPDH structures.

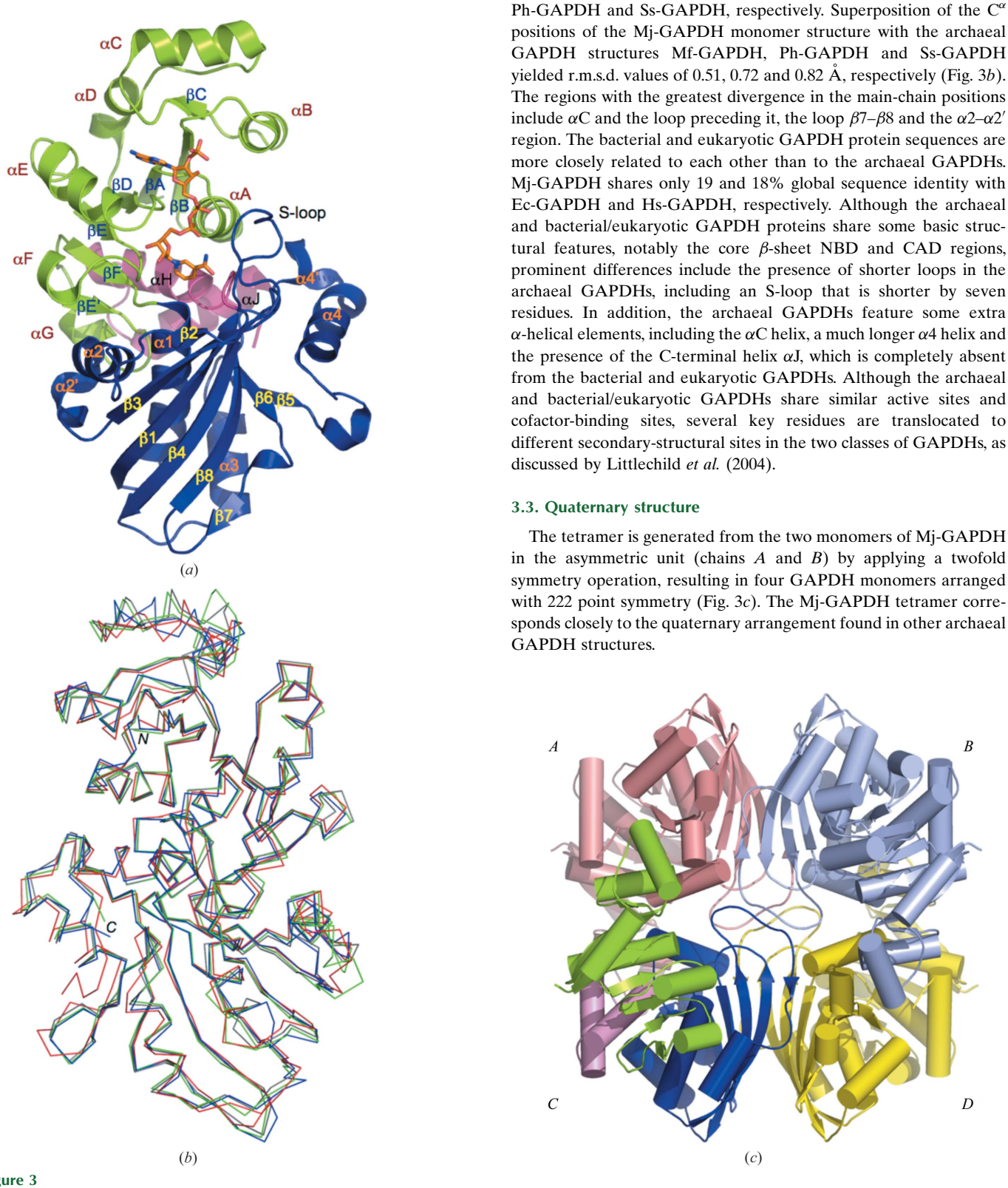

Figure 3
Overall structure of Mj-GAPDH. (*a*) Structure of the Mj-GAPDH monomer. The NBD (residues 1–142) is displayed in green, the CAD (143–305) in blue and the CTD (306–343) in pink. The bound $NADP^{+}$ is depicted as a ball-and-stick model. Secondary-structure elements are indicated. (*b*) Superposition of the C^{α} positions of the monomer structures from four archaeal GAPDH proteins. Mj-GAPDH (PDB code 2yyy) is shown in green, Mf-GAPDH (PDB code 1cf2; Charron *et al.*, 2000) is shown in grey, Ph-GAPDH (PDB code 2czc; K. Ito, R. Arai, T. Kamo-Uchikubo, M. Shirouzu & S. Yokoyama, unpublished work) is shown in blue and Ss-GAPDH (PDB code 1b7g; Isupov *et al.*, 1999) is shown in red. The N- and C-termini are indicated. (*c*) The quaternary structure of Mj-GAPDH. The *C* subunit is coloured as in (*a*).

The Mj-GAPDH tetramer has three intersubunit interfaces. The *AB* interface is composed of the central β-sheets from the catalytic domains of two adjacent monomers and has a surface area of approximately 1700 Å^2 that mostly consists of hydrophobic residues. The *AC* interface is largely α-helical in content, with a surface area of approximately 1400 Å^2. It has been suggested that the high concentration of electrostatic interactions at this interface is a determinant of thermal stability in archaeal GAPDH (Isupov *et al.*, 1999). Notably, two unique hydrogen-bond interactions that occur at the *AC* interface of Mj-GAPDH are not found in other archaeal GAPDHs: those between the side chains of Asp179 and Ser263 and between the side chains of Asp179 and Ser264, both with bond distances of 2.6 Å. The *AD* interface is composed primarily of the S-loops from the two opposite subunits (residues 180–185), with a buried surface area of 440 Å^2. The interactions at the *AD* interface of Mj-GAPDH are similar to those observed in other archaeal GAPDH proteins.

3.4. Stabilization of loops by the C-terminal domain

In the archaeal GAPDH structures the CTD, which includes helices αH and αJ, adopts a wedge-shaped configuration that is situated at the junction between the larger NBD and CAD. The predominantly polar residues of the CTD participate in an extensive network of hydrogen bonds and ion pairs with residues from the two other domains (Fig. 4). Some prominent features of this network include a residue cluster on the NBD composed of Gln24-Asp25-Asp26, which interacts with Arg320 and Lys335 of the CTD. Furthermore, the Arg252 side chain on CAD appears to be crucial for stabilizing the configuration of the CTD, as it forms multiple interactions with both the αH (Glu314, Asp317) and αJ (Ile333, Asn337) helices.

Analysis of the structure reveals that the majority of the electrostatic interactions mediated by the CTD involve partners that lie in the loop regions on either the NBD or CAD (Table 2). In total, 13 different CTD residues participate in interdomain hydrogen-bond or ion-pairing interactions with residues found in ten different loop regions. In general, these interdomain-stabilizing interactions are also conserved in the other archaeal GAPDH structures. In contrast, bacterial and eukaryotic GAPDH structures display only about half the number of polar interactions between the C-terminal region and the distal loop regions, including proteins from thermophilic sources such as *Bacillus stearothermophilus* GAPDH (PDB code 1gd1; Skarzynski *et al.*, 1987). It is hypothesized that the interdomain tethering of loops by the CTD is a strategy adopted by the archaeal GAPDHs in order to reduce the overall protein flexibility and thus enhance hyperthermostability.

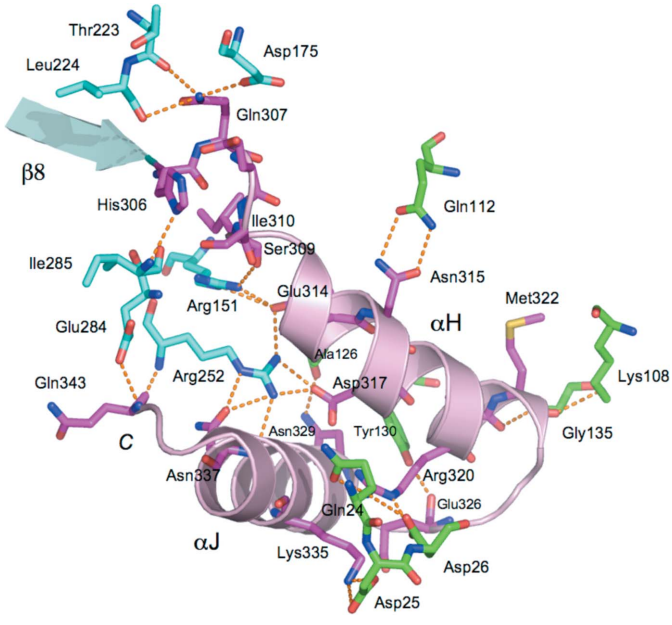

Figure 4
Interdomain interactions involving the C-terminal domain. The network of electrostatic interactions between the CTD and the two other domains is shown. The CTD is shown in pink, NBD residues are in green, and CAD residues are in cyan.

Table 2
Interdomain polar contacts involving the C-terminal domain of Mj-GAPDH.

(*a*) CTD–NDB contacts.

CTD residue	Location	NBD residue	Location
Glu314 OE1	αH	Ala126 N	Loop βE′–αG
Asn315 NE2	αH	Gln112 OE1	Loop βE–αF
Asn315 OE1	αH	Gln112 NE2	Loop βE–αF
Arg320 NE	αH	Asp26 OD2	Loop αA–βB
Arg320 NH2	αH	Gln24 OE1	Loop αA–βB
Arg320 NH2	αH	Asp26 OD1	Loop αA–βB
Ala321 O	αH	Gly135 N	Loop αG–βF
Met322 O	αH	Lys108 NZ	Loop αE–βE
Asn329 ND2	αJ	Ala126 O	Loop βE′–αG
Lys335 NZ	αJ	Asp25 OD1	Loop αA–βB
Lys335 NZ	αJ	Asp25 OD2	Loop αA–βB

(*b*) CTD–CAD contacts.

CTD residue	Location	CAD-residue	Location
His306 ND1	Loop β8–αH	Ile282 N	Loop α4′–β6
Gln307 NE2	Loop β8–αH	Asp175 OD1	S-loop
Gln307 NE2	Loop β8–αH	Thr223 O	Loop β3–β4
Ile310 O	Loop β8–αH	Arg151 NH2	α1
Glu314 OE2	αH	Arg252 NH1	Loop α3–β5
Glu314 OE2	αH	Arg151 NE	α1
Glu314 OE2	αH	Arg151 NH2	α1
Asp317 OD2	αH	Arg252 NH1	Loop α3–β5
Asp317 OD2	αH	Arg252 NH2	Loop α3–β5
Ile333 O	αJ	Arg252 NH2	Loop α3–β5
Asn337 OD1	αJ	Arg252 NE	Loop α3–β5
Asn337 OD1	αJ	Arg252 NH2	Loop α3–β5
Gln343 N	C-terminal loop	Glu284 OE2	Loop α4′–β6
Gln343 O	C-terminal loop	Arg252 N	Loop α3–β5

3.5. Cofactor binding

The NADP$^+$ cofactor is bound at the NBD of the Mj-GAPDH structure (Fig. 5*a*). As in other Rossmann-fold proteins, the NBD contains an N-terminal glycine-rich phosphate-binding loop with the consensus sequence $GX_1GX_2X_3G$ (residues 9–14). This motif provides a hydrogen-bonding network that places the pyrophosphate group of the dinucleotide directly above αA along the helical axis. Hydrogen-bond interactions with the main-chain N atoms of Ser12 and Ile13 directly participate in stabilization of the pyrophosphate. Typical of the motif, this region also features a structurally conserved water molecule coordinated by multiple interactions with the protein and the pyrophosphate of NADP$^+$ (Bottoms *et al.*, 2002).

As in all GAPDH structures, the nicotinamide moiety of NADP$^+$ is held in the *syn* conformation *via* interactions with the conserved residues lying in the N-terminal part of the S-loop. In Mj-GAPDH this involves hydrogen-bond interactions between Arg172 and the nicotinamide carboxymide O7 atom and between Asp175 and the nicotinamide N7 atom.

The structures of Mj-GAPDH and Mf-GAPDH (PDB code 1cf2; Charron *et al.*, 2000) both feature a bound NADP$^+$ cofactor at the NBD. Although the overall orientations of the cofactor are similar, the adenine moiety of the NADP$^+$ adopts different conformations in the two structures (Fig. 5*b*). In Mj-GAPDH the plane of the adenine group of NADP$^+$ is rotated by 20° towards the protein core compared with that in the Mf-GAPDH structure. This difference probably reflects the lack of steric hindrance from Ala89 of Mj-GAPDH, as opposed to Thr86 at the same location in Mf-GAPDH, the side chain of which protrudes toward the adenine. Furthermore, in Mf-GAPDH the βC–αC loop residues Ala54–Pro56, which are located on the opposite side of the adenine group, are shifted outwards compared with the equivalent residues Ala53–Pro55 in Mj-GAPDH. This shift accounts for the largest main-chain divergence between the two conserved structures and is probably necessary to accommodate the different configurations of the adenine rings of NADP$^+$.

3.6. Active site

The Mj-GAPDH structure is unique among the reported archaeal GAPDH structures in that the P_i and P_s sites are not occupied by anions. A structural comparison revealed similarities as well as differences in the positions of the conserved phosphate-binding residues (Fig. 5*c*). On the one hand, the active-site residues Ser143, the catalytic Cys144, Asn145 and His226 share identical orientations in all four known archaeal GAPDH structures (with the exception of the Ss-GAPDH catalytic cysteine thiol group). However, a major difference is that in Mj-GAPDH the imidazole groups of the pair of active-site histidines on helix α2, His197 and His198, are shifted away from the P_i position by 2.1 and 1.3 Å, respectively, compared with the Mf-GAPDH structure. Moreover, the side chain of Arg171 from Mj-GAPDH is shifted slightly towards the P_i-binding cavity compared with the other structures. This suggests that in the archaeal GAPDHs the anion-binding residues may alter their conformations between the unoccupied and occupied P_i states during catalysis.

4. Discussion

There is no single determinant of stability among thermophilic and hyperthermophilic proteins; instead, stability is acquired through combinations of various small alterations in the amino-acid sequences in comparison to their mesophilic protein counterparts. The pathways to thermostability include an increase in buried hydrophobic surface area, a greater number of hydrogen bonds and ion pairs, more disulfide bridges, an increased number of prolines, more intersubunit interactions and oligomerization of subunits, shorter loop regions and the anchoring of loose ends (Vieille & Zeikus, 2001). It has been suggested that in the archaeal GAPDHs increased numbers of ion-pair clusters and more efficient molecular packing play a role in promoting stability (Isupov *et al.*, 1999; Charron *et al.*, 2000). In this study, we propose that in addition the tethering of diverse loops to the C-terminal region *via* extensive ion-pairing and

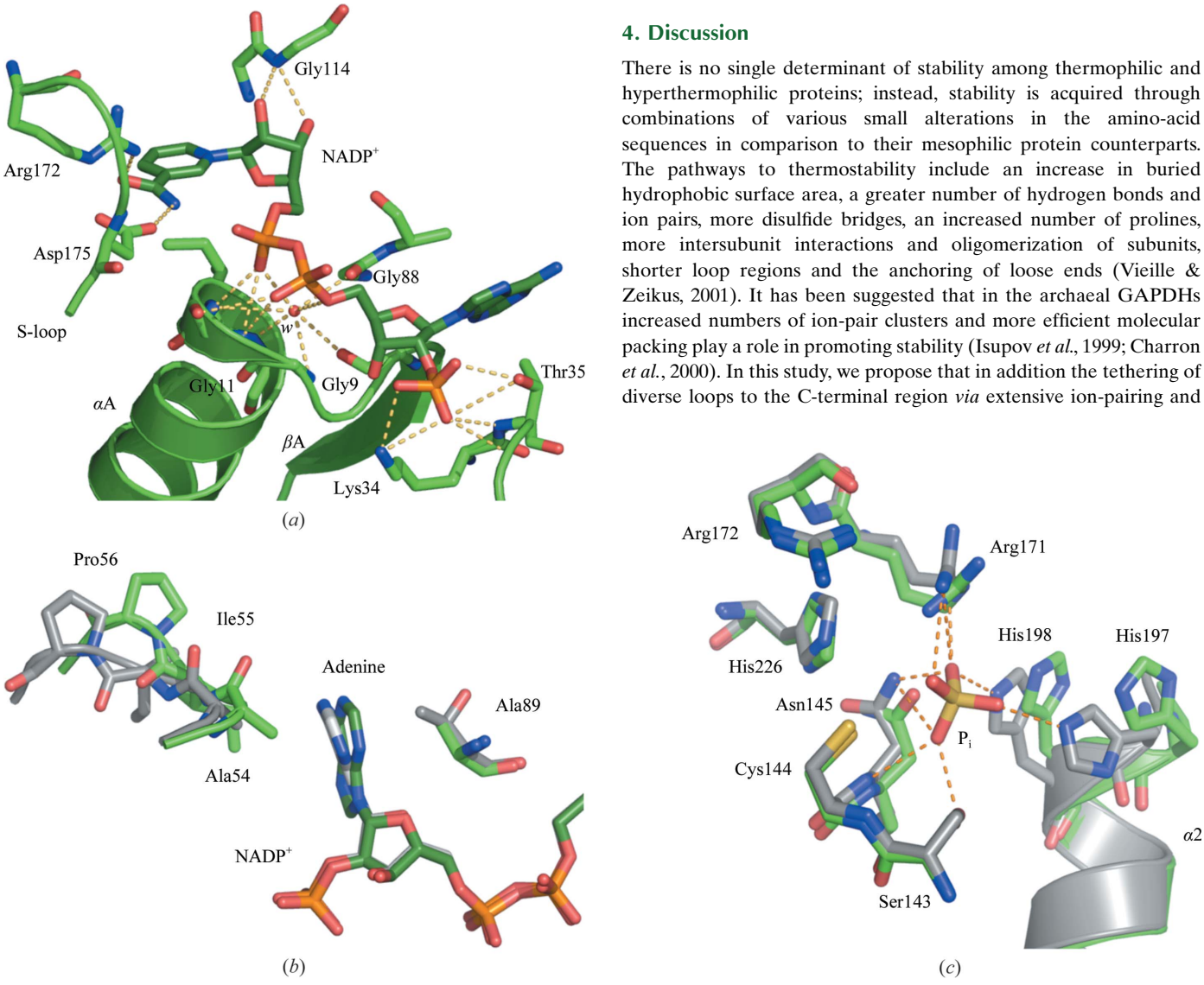

Figure 5
Cofactor-binding and active sites. The Mj-GAPDH structure is shown in green, while Mf-GAPDH is shown in grey. (*a*) The orientation of the bound NADP$^+$ cofactor and its interactions with Mj-GAPDH. Hydrogen-bond interactions are shown as dashed lines and the structurally conserved water molecule is indicated by *w*. (*b*) The different orientations of the adenine moiety of NADP$^+$ in Mj-GAPDH and Mf-GAPDH. Relevant residues from Mj-GAPDH are indicated. (*c*) Differences between the P_i-binding sites of the Mj-GAPDH and Mf-GAPDH structures. The bound sulfate ion from the Mf-GAPDH structure is shown along with its hydrogen-bond interactions with the protein.

hydrogen-bond interactions likewise contributes to increased thermal stability.

We thank Ms Michiyo Takahara, Mr Hitoshi Iino, Mr Yoshihiro Agari and Dr Akio Ebihara for their assistance with sample preparation. We are grateful to Ms Tomoko Nakayama and Ms Azusa Ishii for their clerical assistance. This work was supported in part by the RIKEN Structural Genomics/Proteomics Initiative (RSGI), the National Project on Protein Structural and Functional Analyses, Ministry of Education, Culture, Sports, Science and Technology of Japan. This work was supported by the Synchrotron Radiation Department at the Science and Technology Facilities Council, Daresbury Laboratory UK and beamline 10.1 at the Synchrotron Radiation Source, which was supported by Biotechnology and Biological Sciences Research Council Grant BB/E001971 (to SSH and RWS).

References

Antonyuk, S. V., Eady, R. R., Strange, R. W. & Hasnain, S. S. (2003). *Acta Cryst.* D**59**, 835–842.
Arcari, P., Russo, A. D., Ianniciello, G., Gallo, M. & Bocchini, V. (1993). *Biochem. Genet.* **31**, 241–251.
Bottoms, C. A., Smith, P. E. & Tanner, J. J. (2002). *Protein Sci.* **11**, 2125–2137.
Charron, C., Talfournier, F., Isupov, M. N., Littlechild, J. A., Branlant, G., Vitoux, B. & Aubry, A. (2000). *J. Mol. Biol.* **297**, 481–500.
DeLano, W. L. (2002). *The PyMOL Molecular Graphics System.* DeLano Scientific, San Carlos, California, USA. http://www.pymol.org.
Davis, I. W., Murray, L. W., Richardson, J. S. & Richardson, D. C. (2004). *Nucleic Acids Res.* **32**, W615–W619.
Duée, E., Olivier-Deyris, L., Fanchon, E., Corbier, C., Branlant, G. & Dideberg, O. (1996). *J. Mol. Biol.* **257**, 814–838.
Harris, J. I. & Waters, M. (1976). *The Enzymes*, edited by P. D. Boyer, pp. 1–49. New York: Academic Press.
Isupov, M. N., Fleming, T. M., Dalby, A. R., Crowhurst, G. S., Bourne, P. C. & Littlechild, J. A. (1999). *J. Mol. Biol.* **291**, 651–660.
Jones, T. A., Zou, J.-Y., Cowan, S. W. & Kjeldgaard, M. (1991). *Acta Cryst.* A**47**, 110–119.
Lamzin, V. S. & Wilson, K. S. (1993). *Acta Cryst.* D**49**, 129–147.
Littlechild, J. A., Guy, J. E. & Isupov, M. N. (2004). *Biochem. Soc. Trans.* **32**, 255–258.
Murshudov, G. N., Vagin, A. A. & Dodson, E. J. (1997). *Acta Cryst.* D**53**, 240–255.
Murthy, M. R., Garavito, R. M., Johnson, J. E. & Rossmann, M. G. (1980). *J. Mol. Biol.* **138**, 859–872.
Otwinowski, Z. & Minor, W. (1997). *Methods Enzymol.* **276**, 307–326.
Sirover, M. A. (1999). *Biochim. Biophys. Acta*, **1432**, 159–184.
Sirover, M. A. (2005). *J. Cell. Biochem.* **95**, 45–52.
Skarzynski, T., Moody, P. C. & Wonacott, A. J. (1987). *J. Mol. Biol.* **193**, 171–187.
Tanner, J. J., Hecht, R. M. & Krause, K. L. (1996). *Biochemistry*, **35**, 2597–2609.
Tisdale, E. J. (2002). *J. Biol. Chem.* **277**, 3334–3341.
Vagin, A. & Teplyakov, A. (1997). *J. Appl. Cryst.* **30**, 1022–1025.
Vieille, C. & Zeikus, G. J. (2001). *Microbiol. Mol. Biol. Rev.* **65**, 1–43.
Zheng, L., Roeder, R. G. & Luo, Y. (2003). *Cell*, **114**, 255–266.